Supplementary Information

Treasure-Bowl Style Bifunctional Site in Cerium-Tungsten Hetero-Clusters for Superior Solar-Driven Hydrogen Production

Pengliang Sun[a,c,1], Eduardo Gracia-Espino[b,1], Fang Tan [a,c,1], Hua Zhang[a,c], Qingquan Kong[d], Guangzhi Hu[a,c,*] and Thomas Wågberg[b,e*]

[a] Donghai Laboratory, Zhoushan 316021, China.

[b] Department of Physics, Umeå University, Umeå S-901 87, Sweden.

[c] Institute for Ecological Research and Pollution Control of Plateau Lakes, School of Ecology and Environmental Science, Yunnan University, Kunming 650504, China.

[d] School of Mechanical Engineering, Chengdu University, Chengdu 610106, China.

e Wallenberg Initiative Material Science for Sustainability, Department of Physics, Umeå University, Umeå S-901 87, Sweden.

[1] These authors contributed equally.

*Corresponding author E-mails: guangzhihu@ynu.edu.cn (G.H.) and thomas.wagberg@umu.se (T.W.)

1. Supporting Experimental Section

1.1 Material Preparation

Nickel foam (NF, thickness: 1.5 mm, bulk density: 0.35 g cm^{-3}) was purchased from Changsha Lyrun Mater. Co., Ltd. (Changsha, China). Resorcinol, dopamine (DA), formaldehyde, tetraethyl orthosilicate (TEOS), phosphomolybdic acid hydrate ($H_3[P(W_3O_{10})_4]\cdot xH_2O$, PW_{12}, AR), cerium nitrate hexahydrate ($Ce(NO_3)_3\cdot 6H_2O$), hydrofluoric acid (HF, AR), ethanol (C_2H_5OH, AR) and potassium hydroxide (KOH) purchased from Aladdin Co., Ltd. (Shanghai, China). Commercial Pt/C (20 wt% Pt on Vulcan XC-72R), ruthenium oxide (RuO_2, 99.9 %) and nafion (5 wt %) were purchased from Sigma-Aldrich. All chemicals were used as received without further purification and all aqueous solutions were prepared with ultrapure water (>18.25 MΩ cm^{-1}) obtained from a Millipore system.

1.2 Preparation of SiO_2 Nanospheres

In general, a precisely measured quantity of 20 mL anhydrous ethanol was combined with 4.16 g of ethyl orthosilicate (TEOS) in a 50 mL beaker labeled as beaker A. The contents were carefully stirred until a homogeneous solution was achieved. Subsequently, in a separate 100 mL beaker denoted as beaker B, a mixture composed of 30.6 g of distilled water, 20 mL of anhydrous ethanol, and 6.8 g of ammonia was prepared. This beaker was then placed on a magnetic agitator and stirred continuously. The solution from beaker A was introduced into beaker B in a gradual dropwise manner during the stirring process. The entire mixture was continuously stirred at room temperature for a duration of 6 hours to facilitate the chemical reaction. Upon completion of the reaction period, the resulting solution was separated using centrifugation at a speed of 8500 revolutions per minute. The resultant pure SiO_2 microspheres were subsequently subjected to calcination within a Muffle furnace at a temperature of

800°C for a duration of 3 hours. Following the calcination step, the microspheres were allowed to cool naturally to room temperature.

1.3 Synthesis of WN/WC-CeO_{2-x}@PNC

In the standard synthetic procedure, 1.0 g of silica microspheres was evenly dispersed in a pre-mixed solution containing 100 mL ethanol and deionized water (water: ethanol = 7:3). Subsequently, resorcinol (0.15 g), dopamine (0.1 g), and formaldehyde (0.2 mL) were introduced individually into this solution. After 10 minutes, 0.4 mL of tetraethyl orthosilicate was added, and the mixture was maintained at a controlled temperature with continuous stirring for 14 h. Following this, 0.25 mmol of $H_3[P(W_3O_{10})_4]\cdot xH_2O$ and 0.2 mmol of $Ce(NO_3)_3\cdot 6H_2O$ were incorporated, with further agitation for an additional 10 hours. The resulting precipitate was isolated via centrifugation, followed by three washes with ultrapure water and anhydrous ethanol, concluding with overnight vacuum drying at 60 °C. The resultant product then underwent annealing under an argon atmosphere, initially at 500 °C for 30 minutes, followed by carbonization at 900 °C for 3 hours. Finally, the WN/WC-CeO_{2-x}@PNC catalyst was obtained by etching the silica microspheres with a 5 wt% hydrofluoric acid solution. In accordance with the stoichiometric ratios of metal salts, a series of composite materials were synthesized, denoted as Ce_1-$W_{0.2}$, Ce_1-$W_{0.4}$, Ce_1-$W_{0.6}$, Ce_1-$W_{0.8}$ (WN/WC-CeO_{2-x}@PNC), and Ce_1-W_1.

1.4 Synthesis of WN/WC@PNC

Similar to the aforementioned synthesis of WN/WC-CeO_{2-x}@PNC, the omission of $Ce(NO_3)_3\cdot 6H_2O$ in the procedure leads to the formation of WN/WC@PNC.

1.5 Synthesis of CeO_2

Firstly, 5 mmmoL $Ce(NO_3)_3\cdot 6H_2O$ was accurately dissolved in 35 mL ultra-pure water, and then 6 g NaOH was added to it. After stirring for 30 min, the mixture was transferred to a hydrothermal reactor

with a capacity of 50 mL in polytetrafluoroethylene tank and kept at 100 ^{o}C for 24 h. After the reaction was finished, the product was separated by high speed centrifuge and washed for three times with ultra-pure water and anhydrous ethanol respectively. Finally, the sample was heated to 400 ^{o}C at a rate of 5 min/ ^{o}C and kept for 4 h, and finally CeO_2 was obtained.

1.6 Material Characterization

The SEM images and EDX elemental mapping were obtained with a Hitachi SU8010 scanning electron microscope (Japan). HRTEM (High resolution transmission electron microscopy), SAED (selected area electron diffraction) and STEM (scanning transmission electron microscope) were performed by Thermo Fisher Scientific Talos F200S. Powder X-ray diffraction data (XRD) pattern was recorded on a Rigaku TTRIII-18KW diffractometer operated at 40 kV voltage and 30 mA current using Cu Kα radiation (λ = 1.5418 Å) in the range of 10 - 80^{o}. Raman spectroscopy was recorded using a confocal Raman spectrometer (Renishaw, RM2000) that was operated using an Ar^{+} laser (532 nm wavelength) as the excitation source. The room temperature electron paramagnetic resonance spectroscopy (EPR) spectra were recorded on an X-band (ν_{mw} = 9.84 GHz) EMXmicro BRUKER spectrometer. X-ray photoelectron spectroscopy (XPS) studies were performed by means of a Thermo Fisher K-Alpha^{+} equipped with monochromatic Al Ka radiation (150 W, 5 kV at 1486.6 eV). The chamber pressure for the spectrometer was kept at 10^{-9} Torr. The surface charge was corrected by referencing the spectra to the C 1s peak for the C-C bond at a binding energy of 284.8 eV. Raman spectra of the samples were recorded on a WITec system with a 355 nm excitation wavelength. Specific surface area and corresponding pore size distribution were quantitatively determined by measuring N_2 adsorption-desorption isotherms on a Quantachrome apparatus (Micrometrics, ASAP 2020), using the Brunauer-Emmett-Teller (BET) and Barrett-Joyner-Halenda (BJH) methods, respectively. XAS tests

were performed at the photoemission end-station at beamline BL11B of National Synchrotron Radiation Laboratory (NSRL) in shanghai, China. XAS data extracted and analyzed using the Athena and Artemis codes. Inductively coupled plasma optical emission spectroscopy (ICP-OES, Agilent 5110) was carried out to determine the contents doped into copper in precursor, 5 mg of the sample was completely dissolved into 1 L deionized water with 5 mM HNO_3 and sonicated for 30 min for the ICP-OES test.

1.7 Electrochemical Measurements

Electrochemical measurements were performed using a conventional three-electrode configuration on a CHI 760E electrochemical workstation (CHI Instruments, Inc., Shanghai, China). A graphite rod and a reversible hydrogen electrode were used as the counter electrode and reference electrode, respectively. The catalyst ink was prepared as follows: 5 mg catalyst was suspended in a mixture containing 980 μL water/ethanol (V:V = 1:1) and 20 μL 5 wt% Nafion suspension, followed by 30 min sonication to form a homogeneous ink. 20 μL of the catalyst suspension was deposited onto a carbon paper (CP) with an area of 0.5 cm × 1.0 cm and dried at room temperature. The RuO_2 and 20 wt% Pt/C modified NF electrodes were obtained by the same method. Before the electrochemical experiments, the newly prepared 1.0 M KOH was first bubbled with high-purity Ar (for HER) or O_2 (for OER) for ≈ 30 min and then the electrolyte was blanketed with an N_2/Ar or O_2 atmosphere during the entire testing process. Subsequently, CV scans were conducted in the potential window of −0.477 - 0.523 V versus RHE (for HER) or 1.023 - 2.023 V versus RHE (for OER) for several cycles until stable. Then, the linear sweep voltammetry (LSV) plots were obtained with a scan rate of 5 mV s^{-1}. All the polarization curves were corrected after iR compensation by using the equation: Ecorrected = Emeasured – iR, where i is the current and R is the uncompensated ohmic electrolyte resistance. The HER and OER cycling stability tests were conducted by the corresponding long-term CV tests (3000 cycles), after which the related LSV

curves were recorded and compared with that of their initial LSV curves. All measured potentials were referred to the reversible hydrogen electrode (RHE) using the following equation: E(RHE) = E(Hg/HgO) + 0.059 × pH + 0.098 V and the current densities (j) were normalized by geometric surface area. For the HER, linear sweep voltammetry at a scan rate of 5 mV s^{-1} was conducted in 1 M KOH for all samples, and data were obtained with *iR* compensation of 90 %. Electrochemical impedance spectroscopy (EIS) was carried out from 100 *kHz* to 0.1 *Hz* at the given potential with AC amplitude of 10 mV.

1.8 STH Conversion Efficiency Calculation

For the overall water splitting system that produces hydrogen and oxygen molecules using only commercial GaAs solar power as the input, the solar-to-hydrogen conversion efficiency (*STH*) is defined as:

$$STH = \frac{Chemical\ energy\ output}{Solar\ energy\ input} = \frac{j_{op}\ x\ A\ x\ E_f\ x\ FE_{H2}}{P_s\ x\ A} = \frac{1.23 x j_{op}}{P_s} x100\%$$

Here, j_{op} represents the operating current density of the combined system, A is the effective illuminated area, E_f is the standard thermodynamic potential difference between hydrogen evolution and oxygen evolution half-reactions (1.23 V) that is corresponded to the change of Gibbs free energy of overall water splitting, FE_{H2} is the faradic efficiency for hydrogen evolution that is assumed to be 100% and P_s is the power of solar illumination (AM 1.5G 100 mW cm^{-2}).

1.9 Theoretical calculation

We have employed the first-principles [1,2] to perform all Spin-polarization density functional theory (DFT) calculations within the generalized gradient approximation (GGA) using the Perdew-Burke-Ernzerhof (PBE) [3] formulation. We have chosen the projected augmented wave (PAW) potentials [4,5] to describe the ionic cores and take valence electrons into account using a plane wave basis set with a kinetic energy cutoff of 450 eV. Van der Waals interactions have been considered using

the DFT-D3 method of Grimme [6,7]. The electronic energy was considered self-consistent when the energy change was smaller than 10^{-5} eV. A geometry optimization was considered convergent when the energy change was smaller than 0.02 eV $Å^{-1}$. During the relaxation, the Brillouin zone with a 3 × 3 × 1 Gamma centered grid was used. The 15 Å vacuum layer was normally added to the surface to eliminate the artificial interactions between periodic images. Spin polarized calculations were performed for this calculation.

WC/WN, WC/WN-CeO_2 and WC/WN-CeO_{2-x}-Ov according to the STEM results were employed as the models to further determine the intrinsic mechanism for the excellent catalytic activity. In the vertical direction, a vacuum layer of about 15 Å in thickness was introduced to avoid the interaction between neighboring image structures.

In all the calculations, we use 3×2×1 for the Monkhorst-Pack k-point for periodic crystal structure and surface model. The convergence threshold for energy was set at 10^{-5} eV. [8] The equilibrium lattice constants were optimized with maximum stress on each atom within 0.05 eV/Å. In order to precisely reflect the calculations, the DFT+U corrections for 5d transition metal (W: 6 eV) were employed.[9]

The adsorption energy (ΔE_{ads}) was defined as follows：

$$E_{ads} = E_{ad/sub} - E_{ad} - E_{sub}$$

where $E_{ad/sub}$, E_{ad} and E_{sub} are the optimized adsorbate/substrate system, the adsorbate in the structure and the clean substrate respectively. Usually, a more negative E_{ads} value reflects stronger adsorption.

The free energy was calculated using the equation:

$$\Delta G = \Delta E + \Delta ZPE - \Delta TS$$

Where ΔG, ΔE, ΔZPE, and TS represented the free energy, total energy from DFT calculations, zero-point energy, and entropic contributions (T was set to be 300 K), respectively.

2. Supporting Figures

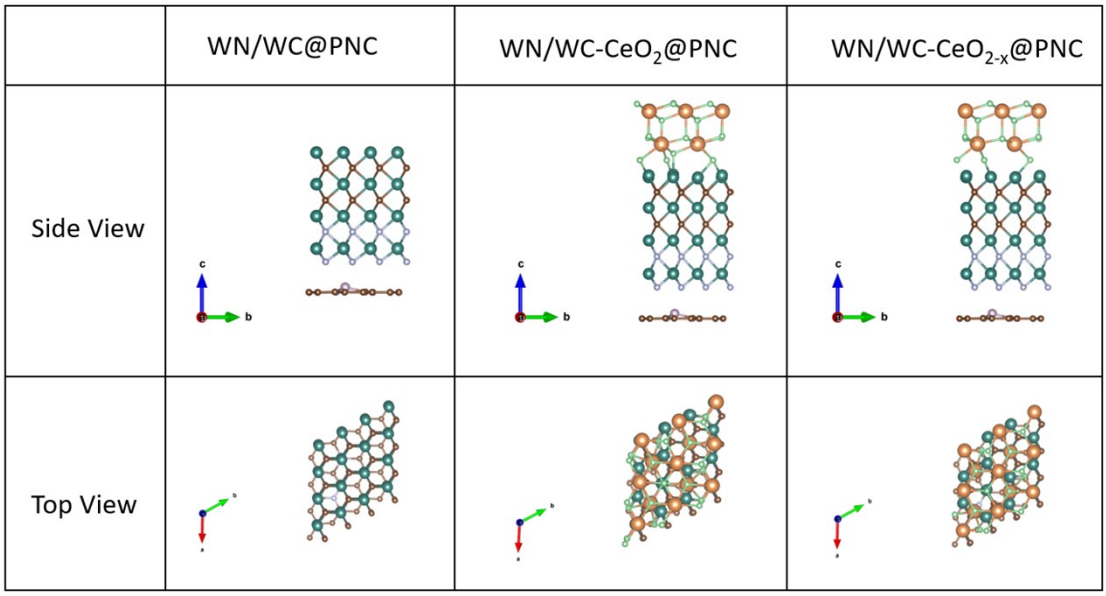

Figure S1. The optimized atomic models of WN/WC@PNC, WN/WC-CeO_2@PNC and WN/WC-CeO_{2-x}@PNC.

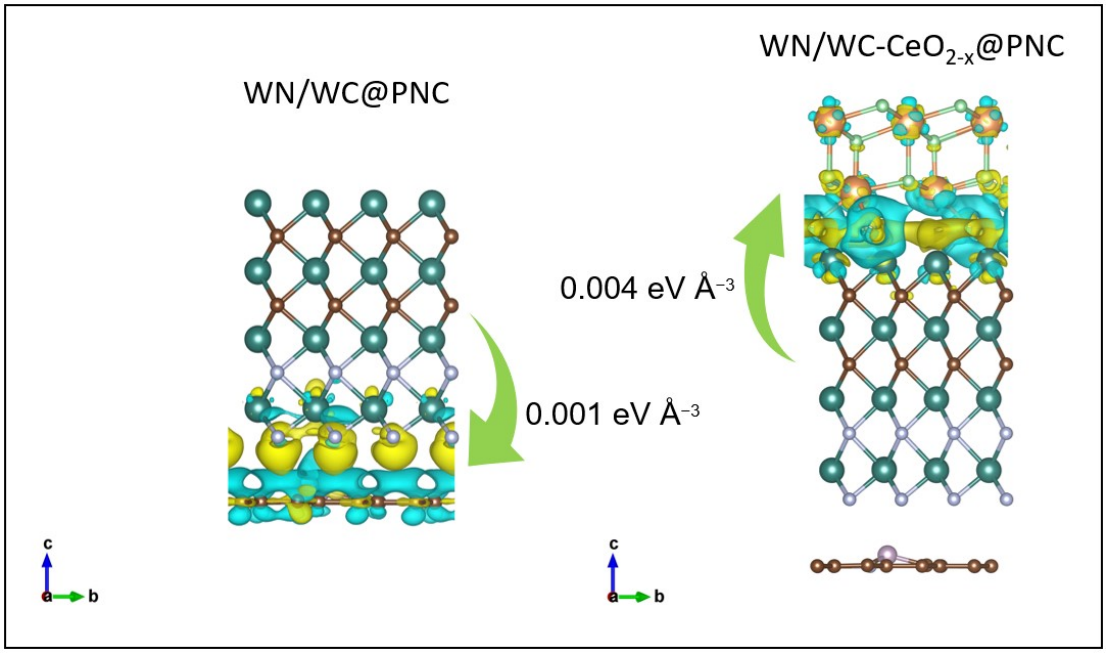

Figure S2. The charge density difference of the WN/WC@PNC and WN/WC-CeO_{2-x}@PNC.

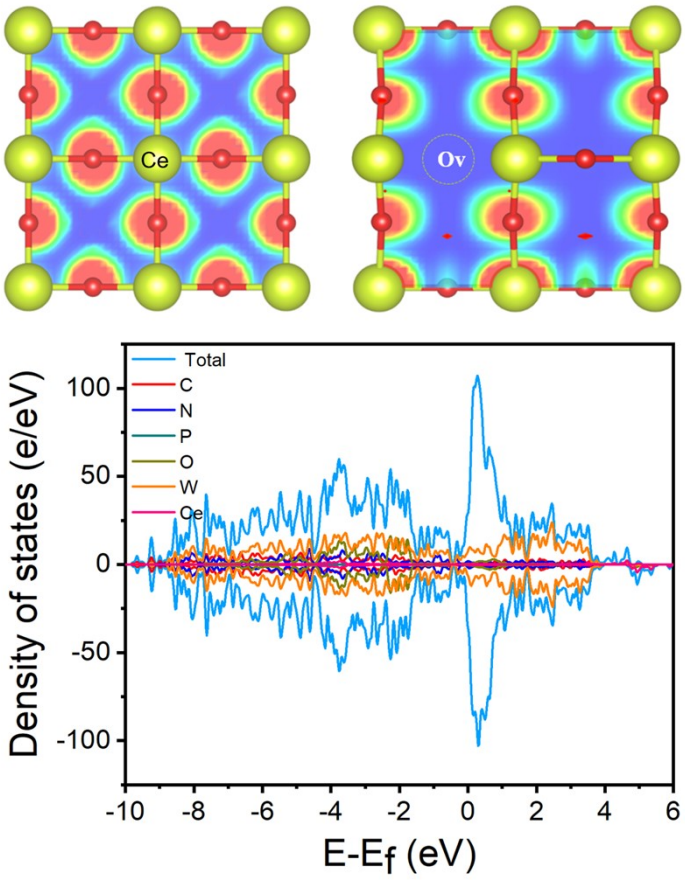

Figure S3. Density of states of WN/WC-CeO_2@PNC.

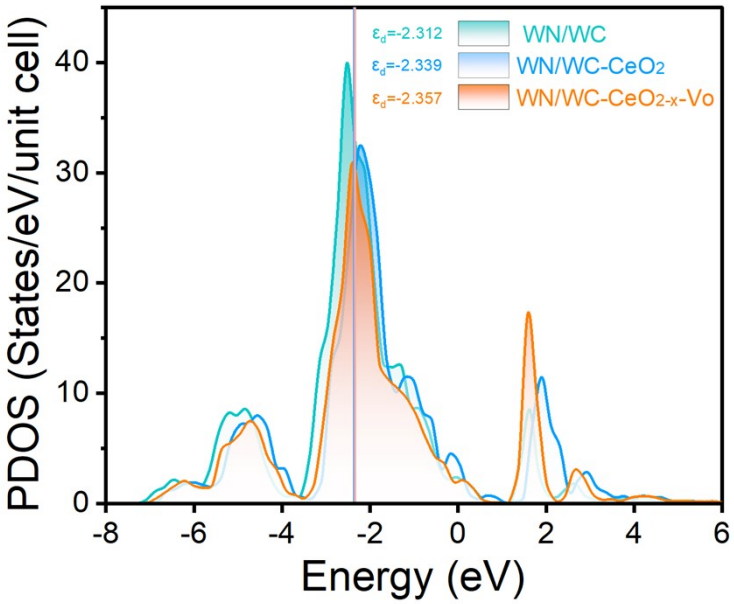

Figure S4. *d*-band centers for WN/WC, WN/WC-CeO_2, and WN/WC-CeO_{2-x}-O_v.

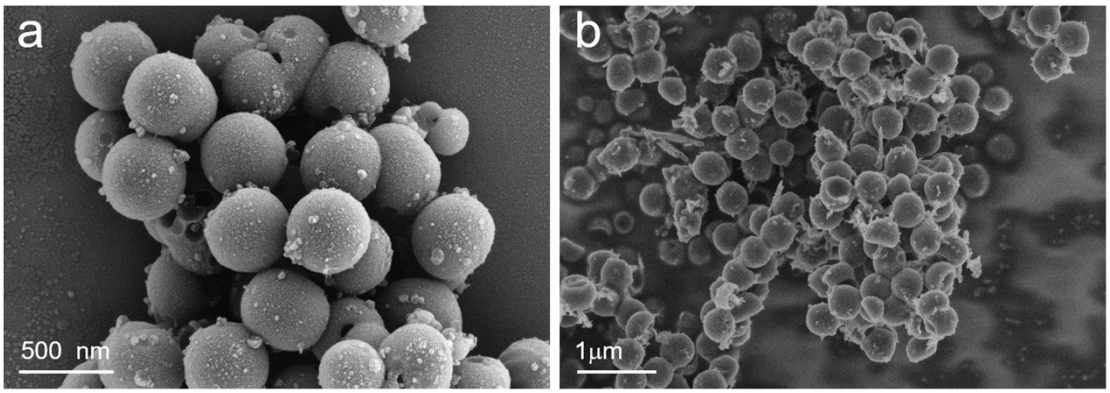

Figure S5. SEM images of (a) SiO_2@Ce-PW_{12}@RF/SiO_2 and (b) SiO_2@WN/WC-CeO_{2-x}@PNC.

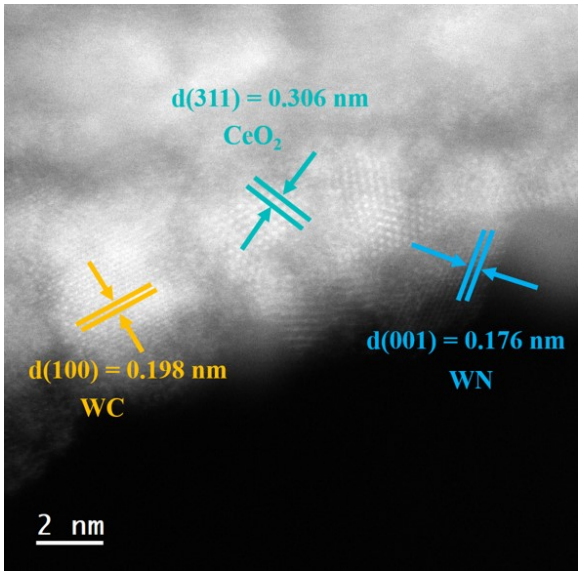

Figure S6. High-resolution TEM images of WN/WC-CeO_{2-x}@PNC.

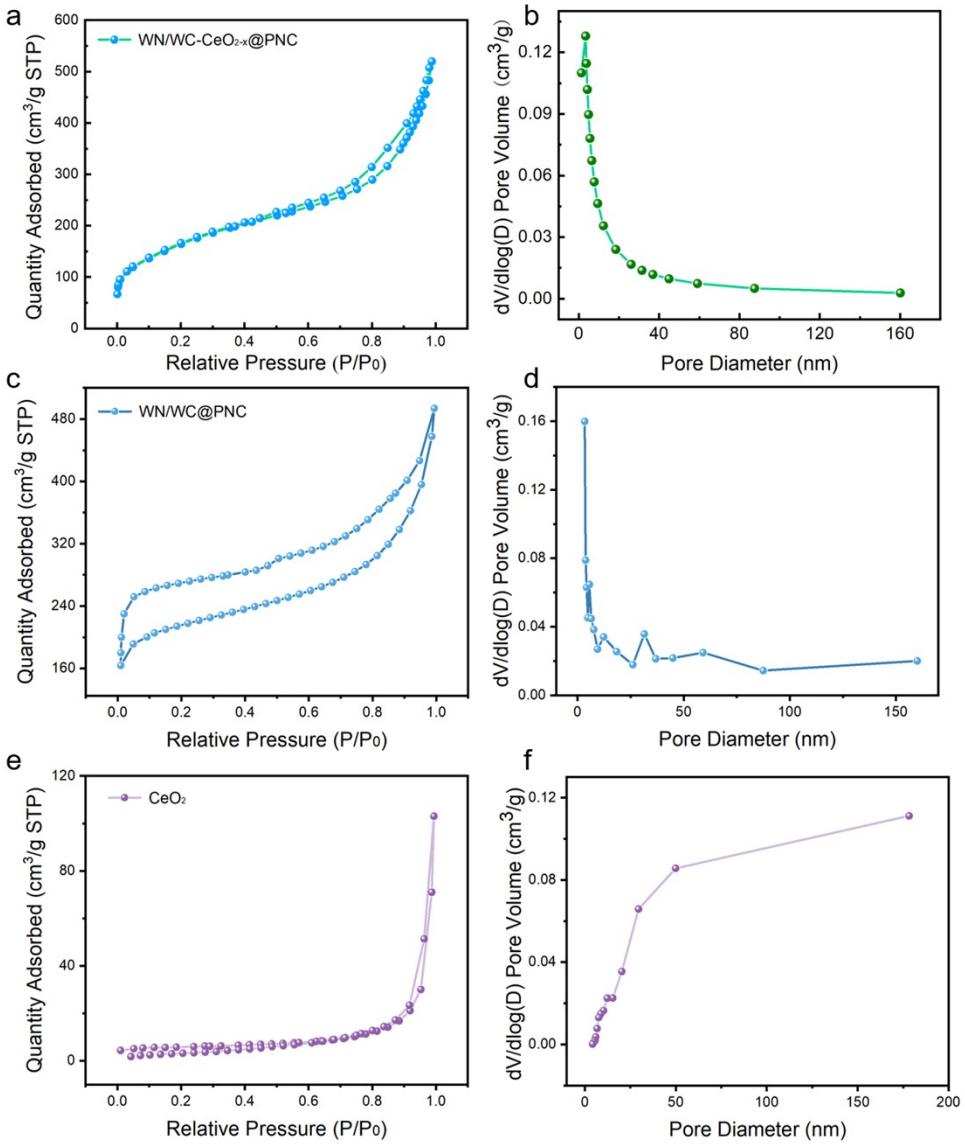

Figure S7. N_2 adsorption–desorption isotherms and (inset) using the BJH (Barrett-Joyner-Halenda) method calculated corresponding pore size distributions of the (a, b) WN/WC-CeO_{2-x}@PNC, (c, d) WN/WC@PNC, and (e, f) CeO_2.

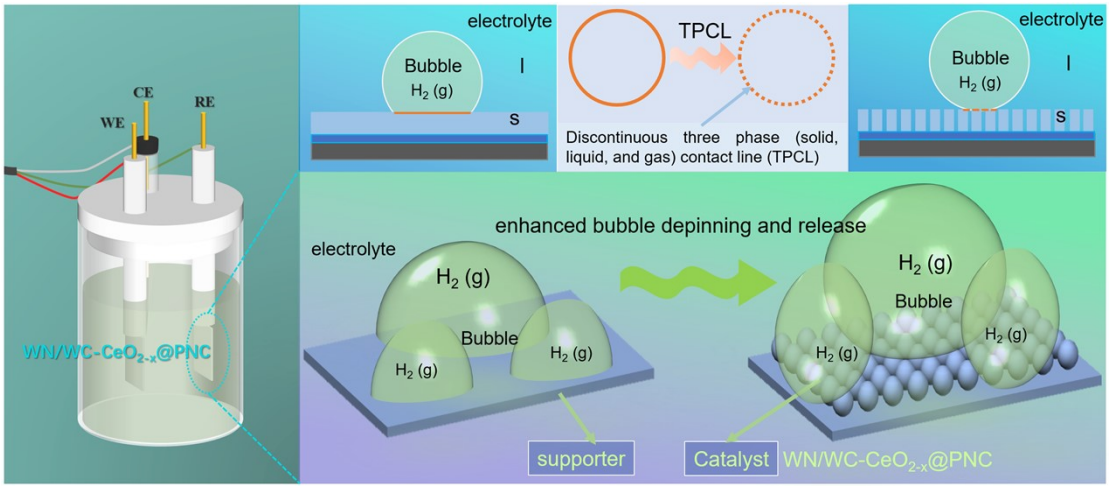

Figure S8. Schematic illustration of how the surface roughness affecting the bubble contact angle at the WN/WC-CeO_{2-x}@PNC clusters.

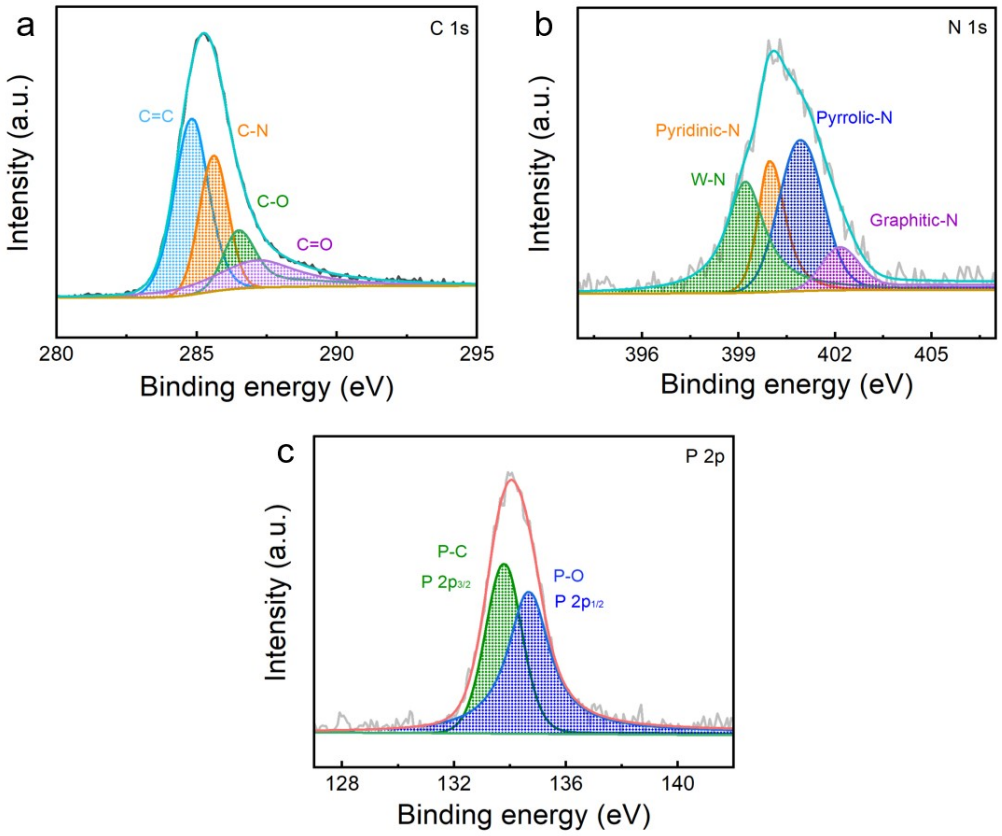

Figure S9. XPS survey spectra and high-resolution (a) C 1s, (b) N 1s, and (c) P 2p, XPS profiles of WN/WC-CeO_{2-x}@PNC.

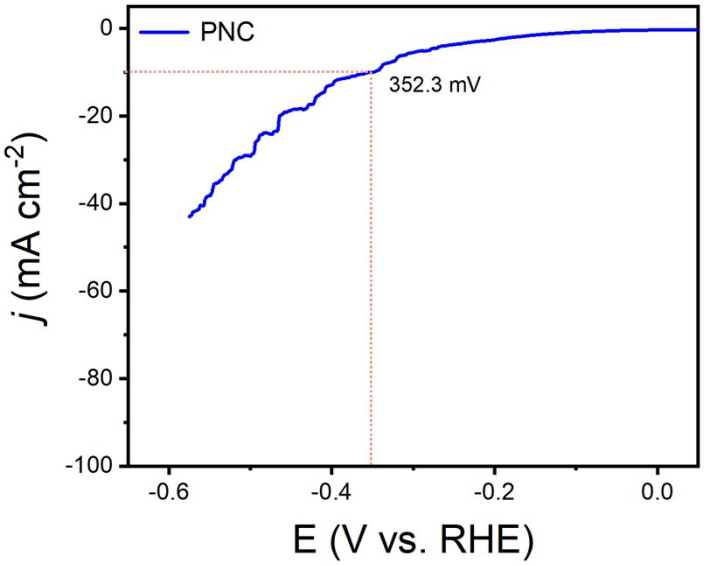

Figure S10. LSV curves of PNC samples in 1.0 M KOH for HER.

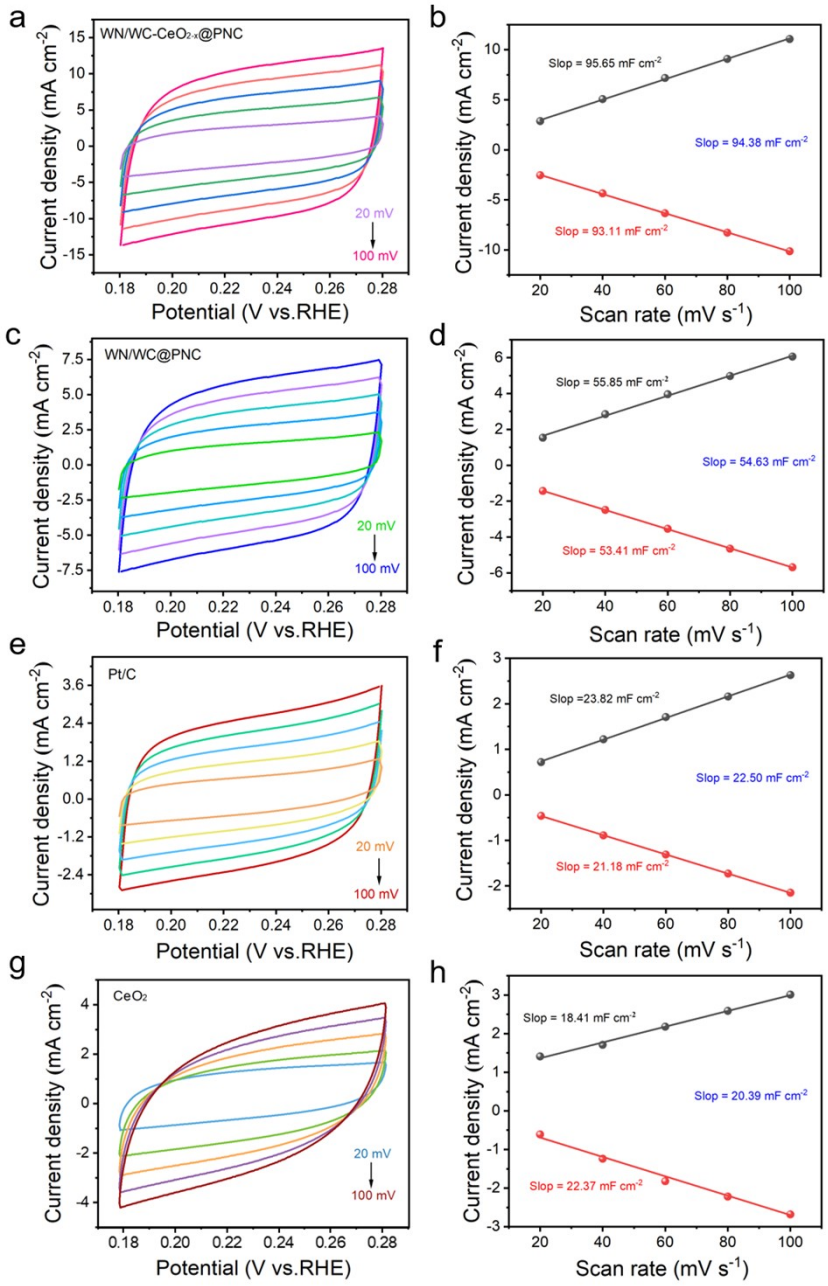

Figure S11. In the non-faradic capacitance current range of 20 to 100 mV s^{-1}, cyclic voltammograms of (a, b) WN/WC-CeO_{2-x}@PNC, (c, d) WN/WC@PNC, (e, f) Pt/C, and (g, h) CeO_2 were recorded.

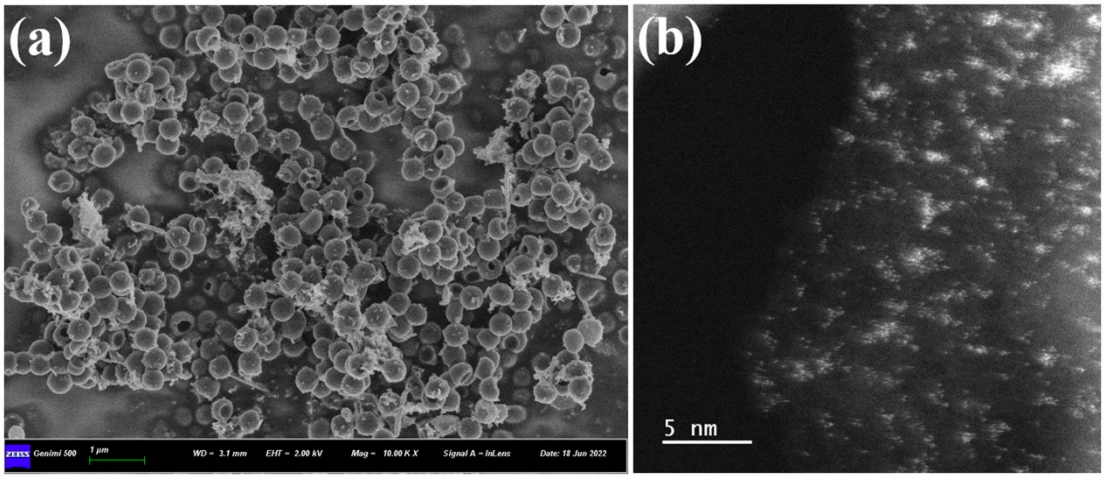

Figure S12. (a) SEM and (b) STEM images of WN/WC-CeO_{2-x}@PNC after the HER durability test at different magnifications.

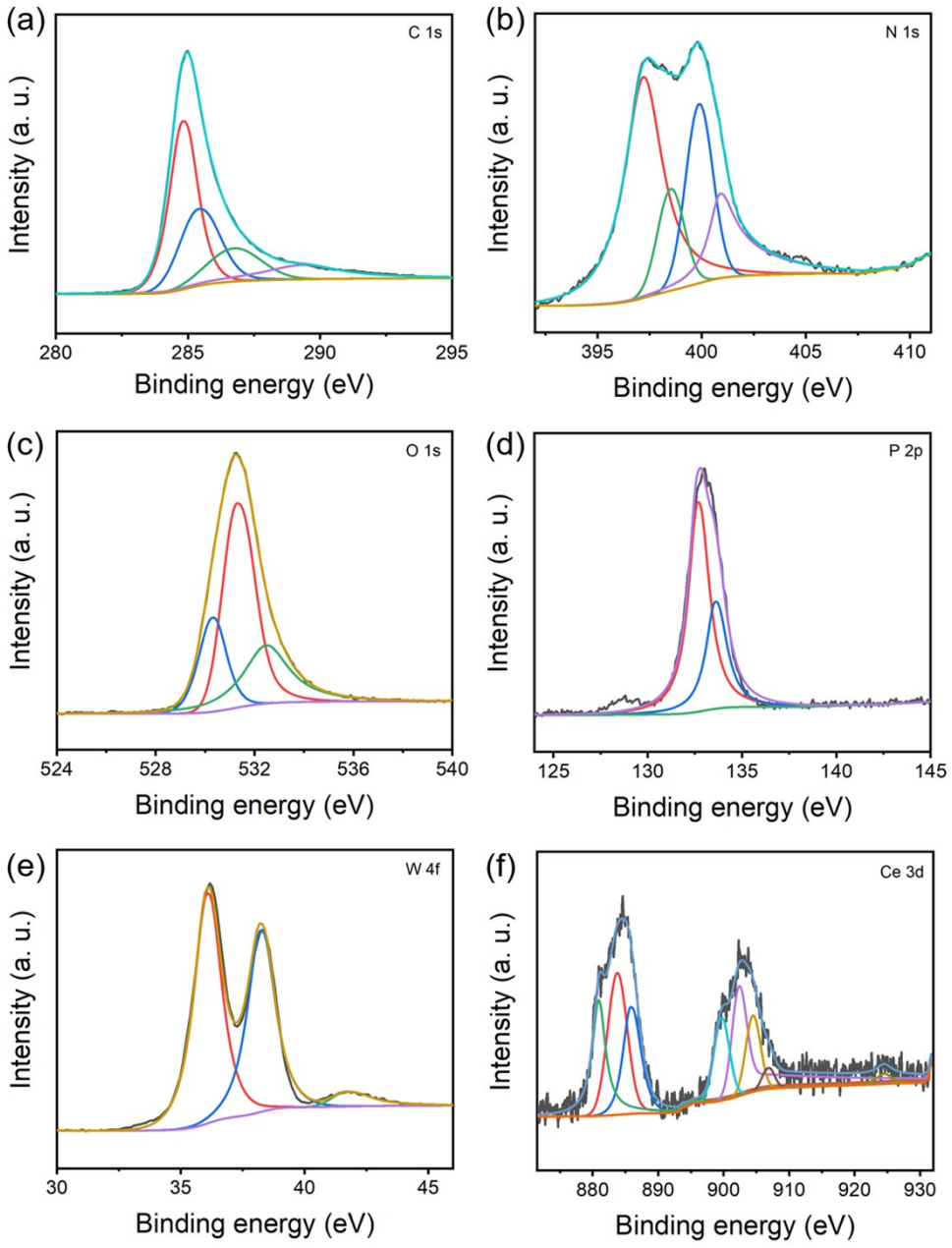

Figure S13. Post characterizations of WN/WC-CeO_{2-x}@PNC catalyst after HER stability test. (a) C 1s, (b) N 1s, (c) O 1s, (d) P 2p, (e) W 4f and (f) Ce 3d core level XPS spectra.

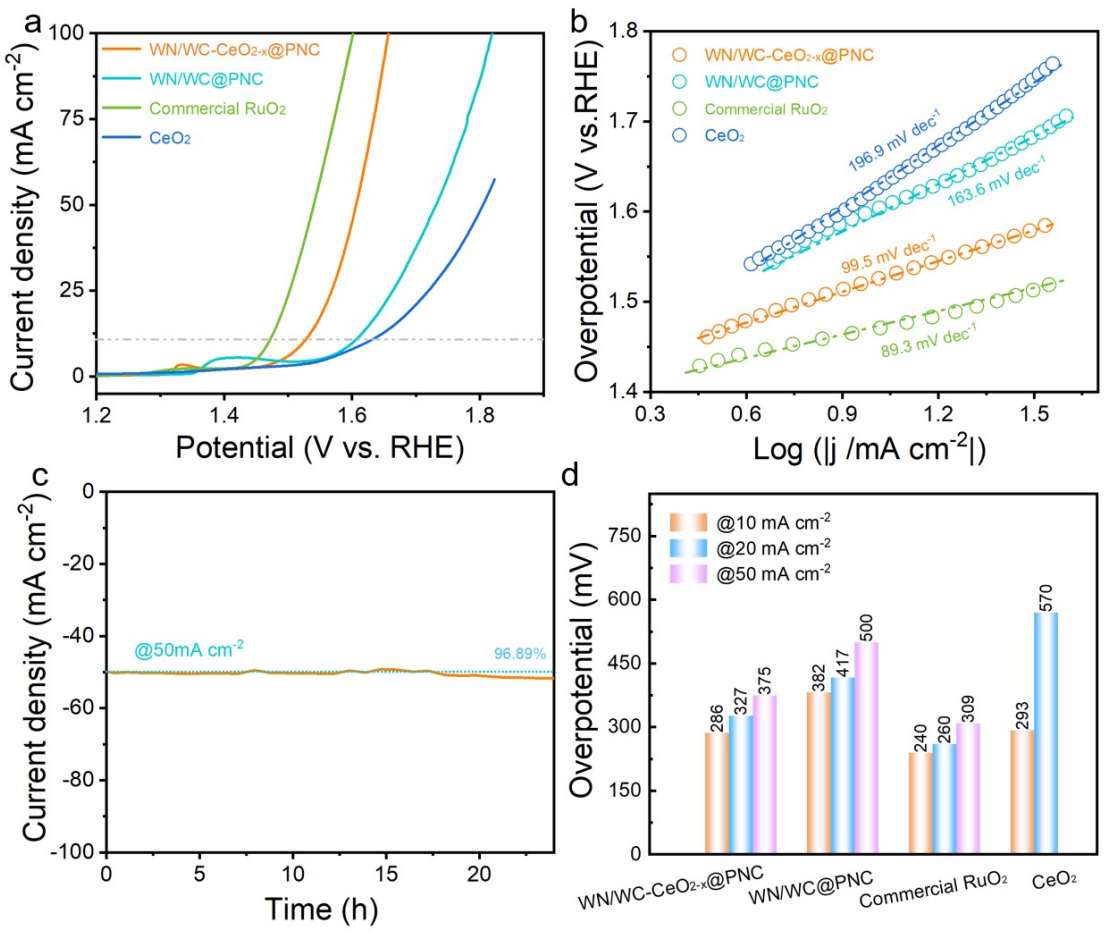

Figure S14. OER catalytic activity evaluation. (a) Polarization curves of all the catalysts for OER. (b) Tafel plots derived from (a) for various catalysts. (c) Chronoamperometric curve of WN/WC-CeO_{2-x}@PNC electrode. (d) Potential requirements at 10, 20 and 50 mA cm^{-2} for all the catalysts.

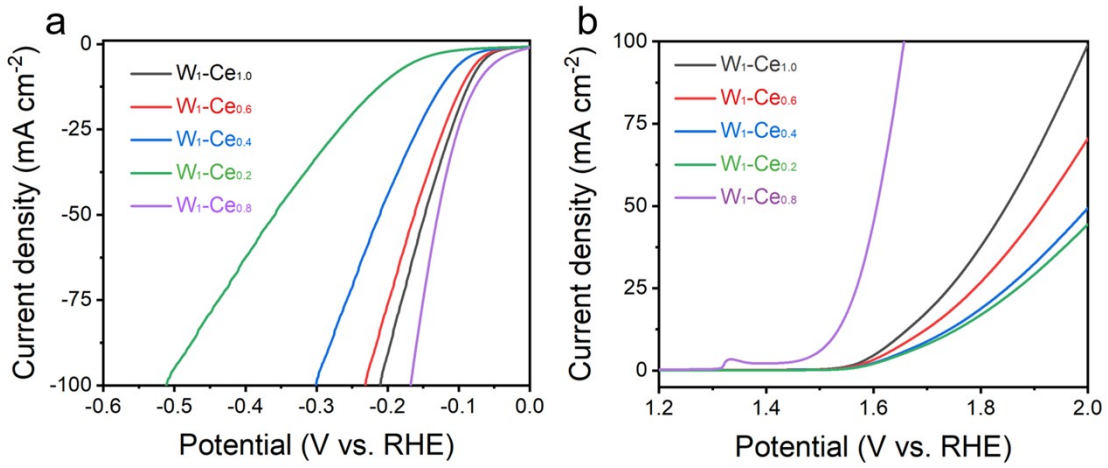

Figure S15. Electrodes with varying W:Ce molar ratios were used for the polarization curves of (a) HER and (b) OER.

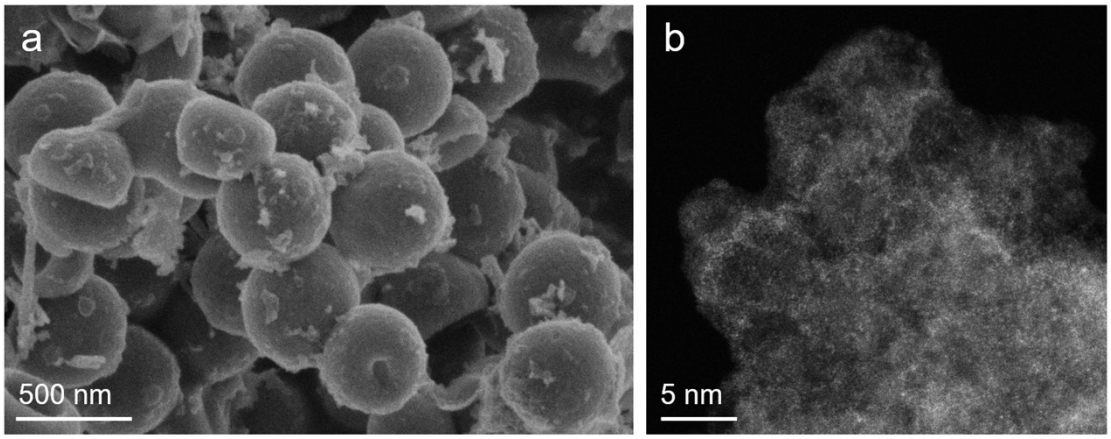

Figure S16. (a) SEM image and (b) STEM image of Ce_1-$W_{0.2}$ catalyst.

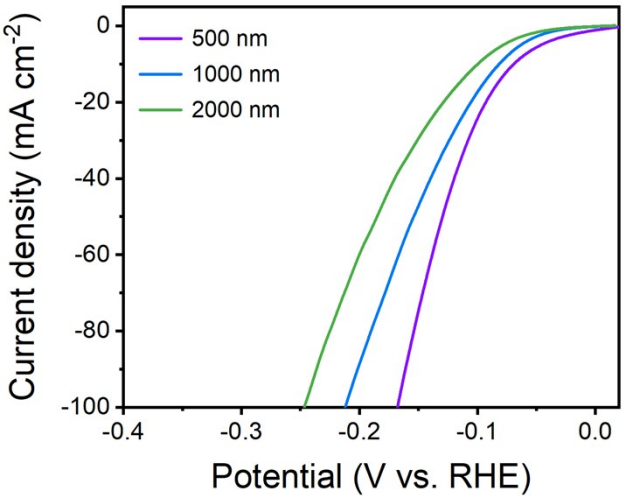

Figure S17. Polarization curves of different sized catalyst electrodes for HER.

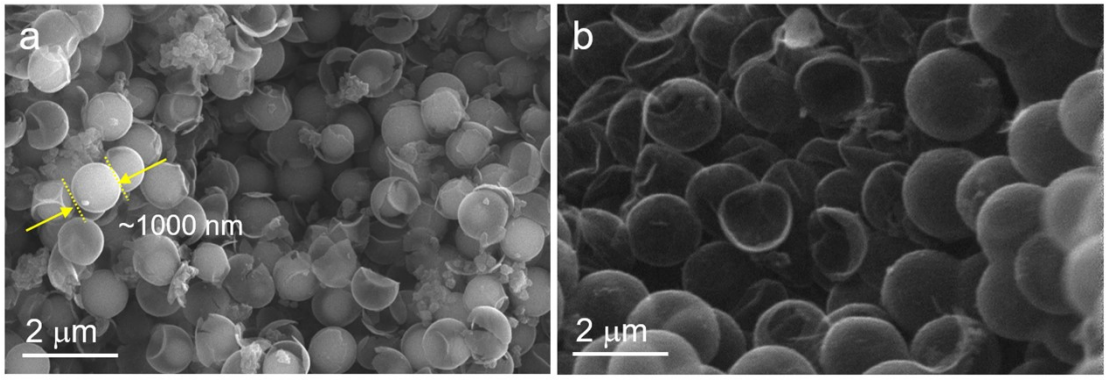

Figure S18. SEM images of Ce_1-$W_{0.8}$ catalysts at different sizes.

3. Supporting Tables

Table S1. Lattice parameters of the samples.

Samples	**Lattice types**	**Lengths(Å)**			**Angles(°)**		
		a	b	c	α	β	γ
WN/WC	P	8.412	8.427	32.000	90	90	119.976
WN/WC-CeO_2	P	8.072	8.080	35.000	90	90	119.988
WN/WC-CeO_{2-x}-O_v	P	8.072	8.080	35.000	90	90	119.988

Table S2. The specific surface area, pore diameter, and pore volume of the sample.

Catalyst	**Surface area (m^2/g)**	**Pore volume (cm^3/g)**	**Average pore (nm)**
WN/WC-CeO_{2-x}@PNC	188.63	0.128	3.123
WN/WC@PNC	120.31	0.113	3.201
CeO_2	36.27	0.085	13.62

Table S3. Metal content of WN/WC-CeO_{2-x}@PNC by ICP-OES.

WN/WC-CeO_{2-x}@PNC	W (wt%)	Ce (wt%)
	8.22 %	1.09 %
post-HER of WN/WC-CeO_{2-x}@PNC	W (mg/L)	Ce (mg/L)
	1.306	0.002

Table S4. HER performances of WN/WC-CeO_{2-x}@PNC and other reported electrocatalysts in the literature.

Catalyst	Electrolyte	η_{10}(mV) (j=10mA cm^{-2})	Tafel slope (mV dec^{-1})	Reference
WN/WC-CeO_{2-x}@PNC	1 M KOH	68.6	39.1	**This work**
Co_2P/WC@NC	1 M KOH	180	90	10
W_2N/WC	1 M KOH	148.5	47.4	11
Cu@WC	1 M KOH	119	88.7	12
WN-Ni@N,P-CNT	1 M KOH	70	151.7	13
Mo_2C-WC/NCA	1 M KOH	126	59	14
Co/WC@NC	1 M KOH	142	91	15
RuO_2-WC NPs	1 M KOH	58	66	16
CeO_2/$Co(OH)_2$ HCs	1 M KOH	309	144	17
WSe_2	1 M KOH	150	78	18
Co/CeO_2/Co_2P/CoP@NC	1 M KOH	195	66	19
WP_2/NF	1 M KOH	130	94	20
Ni–rGO/CeO_2	1 M KOH	113	121	21
VN/WN@NC	1 M KOH	122	67	22
W_2N layer	1 M KOH	232	102	23
N-doped W_2C/WC	1 M KOH	127	62.7	24
W_2C	1 M KOH	274	112	25

Co/WC@NC	1 M KOH	142	91	26
W-W_2C/CNT	1 M KOH	147	51	27
W_2C-NC-WN	1 M KOH	145	96	28
W_2C/WP@NC	1 M KOH	116	59	29
W_2C/C NFs	1 M KOH	81	89	30

Table S5. Overall water splitting performances of WN/WC-CeO_{2-x}@PNC and other reported electrocatalysts in the literature.

Catalyst	Electrolyte	Cell voltage(V) (j=10mA cm^{-2})	Reference
WN/WC-CeO_{2-x}@PNC	1 M KOH	1.55	**This work**
RuO_2-WC NPs	1 M KOH	1.66	31
WN-$Ni(OH)_2$	1 M KOH	1.7	32
WP_2 NW/NF	1 M KOH	1.65	33
W_2C/WP@NC	1 M KOH	1.72	34
WC/Co_3W_3N/Co@NC	1 M KOH	1.61	35
V-CoP@ a-CeO_2	1 M KOH	1.56	36
g-C_3N_4/CeO_2/Fe_3O_4	1 M KOH	1.94	37
Co/CeO_2/Co_2P/CoP@NC	1 M KOH	1.76	38
CeO_2/Ni-TMO	1 M KOH	1.58	39
Co_3S_4/CeO_2-CF	1 M KOH	1.64	40
Pt/C–RuO_2	1 M KOH	1.7	40
$CoWO_4$/CoP_2/CNTF	1 M KOH	1.605	41
NiCoMnFe–P	1 M KOH	1.71	42
NiFe-LDHs@γ-MnOOH	1 M KOH	1.69	43
CeO_2/Co@NCH	1 M KOH	1.74	44
Co_3O_4–CeO_2@FNF	1 M KOH	1.59	45

Table S6. Comparison of *STH* efficiency of reported water splitting systems in the literature.

A systematic comparison of the STH efficiencies reported in the literature confirms the present work achieves the highest reported *STH* efficiency (18.92%) under 1 sun illumination.

Year	Catalyst Cathode/anode	STH (%)	Reference
2015	Pt/RuO_2	8.0	46
2015	$GaInP_2$	8.6	47
2015	Ni-Mo	10.5	48
2016	ZnO:Co	12.7	49
2017	$Na_{0.08}Ni_{0.9}Fe_{0.1}O_2$	11.22	50
2018	NiFe NPs	9.7	51
2018	Ni–Co–S/Ni–Co–P	10.8	52
2019	NiMoFeP	12.3	53
2019	NiFe	17.52	54
2019	$NiCo_2S_4$	18.01	55
2019	CC/TiC/Pt and NiFe LDH	18.7	56
2020	NiFe/carbon nanotube	12.3	57
2021	H-FeNiP	5.57	58
2021	Au- Fe_3O_4/N-TiO_2	11.9	59
2021	$(Co,Fe)PO_4$	12.8	60

2021	WO_3	13	61
2021	NiMP/NF	14	62
2021	Co–NC@CC	15.26	63
2022	p-Ni_5P_4@NF	14.5	64
2022	Co_2P/Mo_2C@NC	18.1	65
2023	Er-NiCoP/NF	19.6	66
2023	$NiFe(OH)_x$–Ni_3S_2/NF	20.05	67
2023	NiFeO-CeO_2/NF	20.1	68
2023	WN/WC-CeO_{2-x}@PNC	18.92	**This work**

4. Supporting References

[1] Kresse, G.; Furthmüller, J. Efficiency of Ab-Initio Total Energy Calculations for Metals and Semiconductors Using a Plane-Wave Basis Set. Comput. Mater. Sci. 1996, 6, 15−50.

[2] Kresse, G.; Furthmüller, J. Efficient Iterative Schemes for Ab Initio Total-Energy Calculations Using a Plane-Wave Basis Set. Phys. Rev. B 1996, 54, 11169−11186.

[3] Perdew, J. P.; Burke, K.; Ernzerhof, M. Generalized Gradient Approximation Made Simple. Phys. Rev. Lett. 1996, 77, 3865−3868.

[4] Kresse G, Joubert D. From ultrasoft pseudopotentials to the projector augmented-wave method[J]. Physical review b, 1999, 59(3): 1758.

[5] Blöchl P E. Projector augmented-wave method[J]. Physical review B, 1994, 50(24): 17953.

[6] Grimme S, Antony J, Ehrlich S, et al. A consistent and accurate ab initio parametrization of density functional dispersion correction (DFT-D) for the 94 elements H-Pu[J]. The Journal of chemical physics, 2010, 132(15).

[7] Grimme S, Ehrlich S, Goerigk L. Effect of the damping function in dispersion corrected density functional theory[J]. Journal of computational chemistry, 2011, 32(7): 1456-1465.

[8] Hurtado-Aular O, Anez R, Sierraalta A. DFT+ U study of the electronic structure changes of WO_3 monoclinic and hexagonal surfaces upon Cu, Ag, and Au adsorption. Applications for CO adsorption[J]. Surface Science, 2021, 714: 121907.

[9] Tan F, Zhou Y, Zhang H, et al. Improving the hydrogen evolution reaction activity of molybdenum-based heterojunction nanocluster capsules via electronic modulation by erbium–nitrogen–phosphorus ternary doping[J]. Chemical Engineering Journal, 2023, 454: 140079.

[10] Gao Y, Lang Z, Yu F, et al. A Co_2P/WC Nano-Heterojunction Covered with N-Doped Carbon as Highly Efficient Electrocatalyst for Hydrogen Evolution Reaction[J]. ChemSusChem, 2018, 11(6): 1082-1091.

[11] Diao J, Qiu Y, Liu S, et al. Interfacial engineering of W_2N/WC heterostructures derived from solid-state synthesis: a highly efficient trifunctional electrocatalyst for ORR, OER, and HER[J]. Advanced Materials, 2020, 32(7): 1905679.

[12]Yao M, Wang B, Sun B, et al. Rational design of self-supported Cu@ WC core-shell mesoporous nanowires for pH-universal hydrogen evolution reaction[J]. Applied Catalysis B: Environmental, 2021, 280: 119451.

[13] Zhang Q, Luo F, Long X, et al. N, P doped carbon nanotubes confined WN-Ni Mott-Schottky heterogeneous electrocatalyst for water splitting and rechargeable zinc-air batteries[J]. Applied Catalysis B: Environmental, 2021, 298: 120511.

[14] Zhang X, Zhu Z, Liang X, et al. Encapsulating dual-phased Mo_2C-WC nanocrystals into ultrathin carbon nanosheet assemblies for efficient electrocatalytic hydrogen evolution[J]. Chemical Engineering Journal, 2021, 408: 127270.

[15] Xu C, Li J, Sun D, et al. Co/WC@NC electrocatalysts derived from polyoxometalates (POM) for efficient hydrogen evolution[J]. Nanotechnology, 2021, 32(37): 375602.

[16] Sun S C, Jiang H, Chen Z Y, et al. Bifunctional WC-Supported RuO_2 Nanoparticles for Robust Water Splitting in Acidic Media[J]. Angewandte Chemie International Edition, 2022, 61(21): e202202519.

[17] Sung M C, Lee G H, Kim D W. CeO_2/$Co(OH)_2$ hybrid electrocatalysts for efficient hydrogen and oxygen evolution reaction[J]. Journal of Alloys and Compounds, 2019, 800: 450-455.

[18] Wang X, Chen Y, Zheng B, et al. Graphene-like WSe_2 nanosheets for efficient and stable hydrogen evolution[J]. Journal of Alloys and Compounds, 2017, 691: 698-704.

[19] Song X Z, Su Q F, Li S J, et al. Heterostructural Co/CeO_2/Co_2P/CoP@ NC dodecahedrons derived from CeO_2-inserted zeolitic imidazolate framework-67 as efficient bifunctional electrocatalysts for overall water splitting[J]. International Journal of Hydrogen Energy, 2020, 45(55): 30559-30570.

[20] Meng F, Yu Y, Sun D, et al. Three-dimensional flower-like WP_2 nanowire arrays grown on Ni foam for full water splitting[J]. Applied Surface Science, 2021, 546: 148926.

[21] Xu Y, Hao X, Zhang X, et al. Increasing oxygen vacancies in CeO_2 nanocrystals by Ni doping and reduced graphene oxide decoration towards electrocatalytic hydrogen evolution[J]. CrystEngComm, 2022, 24(18): 3369-3379.

[22] He D, Cao L, Huang J, et al. Synergistic coupling of heterogeneous VN/WN nanoparticles embedded in N-doped carbon matrix for efficient hydrogen evolution reaction[J]. Chemical Engineering Journal, 2022, 429: 131945.

[23] Hong Z, Xu Z, Wu Z, et al. Construction of core–shell Co-NC@W_2N Schottky heterojunctions for high-efficiency hydrogen evolution reaction[J]. Applied Surface Science, 2023, 608: 155159.

[24] Deng X C, Chang H Q, Zhang G H. N-doped graphene supported W_2C/WC as efficient electrocatalyst for hydrogen evolution reaction[J]. International Journal of Hydrogen Energy, 2022, 47(2): 902-916.

[25] Chen Z, Gong W, Cong S, et al. Eutectoid-structured WC/W_2C heterostructures: A new platform for long-term alkaline hydrogen evolution reaction at low overpotentials[J]. Nano Energy, 2020, 68: 104335.

[26] Xu C, Li J, Sun D, et al. Co/WC@NC electrocatalysts derived from polyoxometalates (POM) for efficient hydrogen evolution[J]. Nanotechnology, 2021, 32(37): 375602.

[27] Hu Y, Yu B, Ramadoss M, et al. Scalable synthesis of heterogeneous W–W_2C nanoparticle-embedded CNT networks for boosted hydrogen evolution reaction in both acidic and alkaline media[J]. ACS Sustainable Chemistry & Engineering, 2019, 7(11): 10016-10024.

[28] Abbas S C, Wu J, Huang Y, et al. Novel strongly coupled tungsten-carbon-nitrogen complex for efficient hydrogen evolution reaction[J]. international journal of hydrogen energy, 2018, 43(1): 16-23.

[29] Wei P, Sun X, Wang M, et al. Construction of an N-Decorated Carbon-Encapsulated W_2C/WP Heterostructure as an Efficient Electrocatalyst for Hydrogen Evolution in Both Alkaline and Acidic Media[J]. ACS Applied Materials & Interfaces, 2021, 13(45): 53955-53964.

[30] Yuan X, Huang W, Kong L, et al. Ditungsten carbide nanoparticles homogeneously embedded in carbon nanofibers for efficient hydrogen production[J]. Chemical Engineering Journal, 2021, 420: 130480.

[31] Sun S C, Jiang H, Chen Z Y, et al. Bifunctional WC-Supported RuO_2 Nanoparticles for Robust Water Splitting in Acidic Media[J]. Angewandte Chemie International Edition, 2022, 61(21): e202202519.

[32] Lv C, Wang X, Gao L, et al. Triple functions of Ni $(OH)_2$ on the surface of WN nanowires remarkably promoting electrocatalytic activity in full water splitting[J]. ACS Catalysis, 2020, 10(22): 13323-13333.

[33] Meng F, Yu Y, Sun D, et al. Three-dimensional flower-like WP_2 nanowire arrays grown on Ni foam for full water splitting[J]. Applied Surface Science, 2021, 546: 148926.

[34] Wei P, Sun X, Wang M, et al. Construction of an N-Decorated Carbon-Encapsulated W_2C/WP Heterostructure as an Efficient Electrocatalyst for Hydrogen Evolution in Both Alkaline and Acidic Media[J]. ACS Applied Materials & Interfaces, 2021, 13(45): 53955-53964.

[35] Li S, Xu C, Zhou Q, et al. Rational design of self-supported WC/Co_3W_3N/Co@ NC yolk/shell nitrogen-doped porous carbon catalyst for highly efficient overall water splitting[J]. Journal of Alloys and Compounds, 2022, 902: 163627.

[36] Yang L, Liu R, Jiao L. Electronic redistribution: construction and modulation of interface engineering on CoP for enhancing overall water splitting[J]. Advanced Functional Materials, 2020, 30(14): 1909618.

[37] Rashid J, Parveen N, Haq T, et al. g-C_3N_4/CeO_2/Fe_3O_4 Ternary Composite as an Efficient Bifunctional Catalyst for Overall Water Splitting[J]. ChemCatChem, 2018, 10(24): 5587-5592.

[38] Song, Xue-Zhi, et al. Heterostructural Co/CeO_2/Co_2P/CoP@ NC dodecahedrons derived from CeO_2-inserted zeolitic imidazolate framework-67 as efficient bifunctional electrocatalysts for overall water splitting. International Journal of Hydrogen Energy 45.55 (2020): 30559-30570.

[39] Long, Xia, et al. Enhancing full water-splitting performance of transition metal bifunctional electrocatalysts in alkaline solutions by tailoring CeO_2–transition metal oxides–Ni nanointerfaces. ACS Energy Letters 3.2 (2018): 290-296.

[40] Feng Z, Pu J, Liu M, et al. Facile construction of hierarchical Co_3S_4/CeO_2 heterogeneous nanorod array on cobalt foam for electrocatalytic overall water splitting. Journal of Colloid and Interface Science, 2022, 613: 806-813.

[41] Wu Q, Sheng M, Shi J, et al. $CoWO_4$/CoP_2 nanoflakes grown on carbon nanotube film as an efficient electrocatalyst for water splitting in alkaline media. Applied Surface Science, 2020, 514: 145919.

[42] Hasan M M, Gomaa A K, Khedr G E, et al. Highly Durable Compositionally Variant Bifunctional Tetrametallic Ni–Co–Mn–Fe Phosphide Electrocatalysts Synthesized by a Facile Electrodeposition Method for High-Performance Overall Water Splitting[J]. Energy & Fuels, 2022.

[43] Wang S B, Xia Y S, Xin Z F, et al. Fabrication of the novel NiFe-LDHs@ γ-MnOOH nanorod electrocatalyst for effective water oxidation[J]. Catalysis Communications, 2022: 106564.

[44] Yu Y, Liu Y, Peng X, et al. A multi-shelled CeO_2/Co@ N-doped hollow carbon microsphere as a trifunctional electrocatalyst for a rechargeable zinc–air battery and overall water splitting[J]. Sustainable Energy & Fuels, 2020, 4(10): 5156-5164.

[45] Liu M, Chen T, Zhang W, et al. In situ construction of pollen-petal-like heterostructured Co_3O_4–CeO_2 on 3D $FeNi_3$ foam as a bifunctional catalyst for overall water splitting[J]. Sustainable Energy & Fuels, 2021, 5(7): 2181-2189.

[46] Nordmann S, Berghoff B, Hessel A, et. al. A monolithic all-silicon multi-junction solar device for direct water splitting. Renewable Energy 2015; 94: 90-95.

[47] Verlage E, Hu S, Liu R, et al. A monolithically integrated, intrinsically safe, 10% efficient, solar-driven water-splitting system based on active, stable earth-abundant electrocatalysts in conjunction with tandem III–V light absorbers protected by amorphous TiO_2 films[J]. Energy & Environmental Science, 2015, 8(11): 3166-3172.

[48] Verlage E, Hu S, Liu R, et. al. A monolithically integrated, intrinsically safe, 10% efficient, solar-driven water-splitting system based on active, stable earth-abundant electrocatalysts in conjunction with tandem III–V light absorbers protected by amorphous TiO_2 films. *Energy Environ Sci.* **2015**, **8**(11): 3166-3172.

[49] Kirner S, Sarajan H, Azarpira A, et. al. Wafer Surface Tuning for a-Si:H/μc-Si:H/c-Si Triple Junction Solar Cells for Application in Water Splitting. Energy Procedia 2016; 102: 126-135.

[50] Weng B, Xu F, Wang C, et al. A layered $Na_{1-x}Ni_yFe_{1-y}O_2$ double oxide oxygen evolution reaction electrocatalyst for highly efficient water-splitting[J]. Energy & Environmental Science, 2017, 10(1): 121-128.

[51] Kumar A, Chaudhary D K, Parvin S, et al. High performance duckweed-derived carbon support to anchor NiFe electrocatalysts for efficient solar energy driven water splitting[J]. Journal of Materials Chemistry A, 2018, 6(39): 18948-18959.

[52] Zhou X, Zhou J, Huang G, et al. A bifunctional and stable Ni–Co–S/Ni–Co–P bistratal electrocatalyst for 10.8%-efficient overall solar water splitting[J]. Journal of Materials Chemistry A, 2018, 6(41): 20297-20303.

[53] Baek M, Kim G W, Park T, et al. NiMoFe and NiMoFeP as complementary electrocatalysts for efficient overall water splitting and their application in PV-Electrolysis with STH 12.3%[J]. Small, 2019, 15(49): 1905501.

[54] Park H, Park I J, Lee M G, et al. Water splitting exceeding 17% solar-to-hydrogen conversion efficiency using solution-processed Ni-based electrocatalysts and perovskite/Si tandem solar cell[J]. ACS applied materials & interfaces, 2019, 11(37): 33835-33843.

[55] Kang Z, Guo H, Wu J, et al. Engineering an Earth-Abundant Element-Based Bifunctional Electrocatalyst for Highly Efficient and Durable Overall Water Splitting[J]. Advanced Functional Materials, 2019, 29(9): 1807031.

[56] Gao J, Sahli F, Liu C, et al. Solar water splitting with perovskite/silicon tandem cell and TiC-supported Pt nanocluster electrocatalyst[J]. Joule, 2019, 3(12): 2930-2941.

[57] Li Z, Wu S, Zhang J, et al. Hybrid perovskite-organic flexible tandem solar cell enabling highly efficient electrocatalysis overall water splitting[J]. Advanced Energy Materials, 2020, 10(18): 2000361.

[58] Zhang R, Wang G, Wei Z, et al. A Fe–Ni_5P_4/Fe–Ni_2P heterojunction electrocatalyst for highly efficient solar-to-hydrogen generation[J]. Journal of Materials Chemistry A, 2021, 9(2): 1221-1229.

[59] Li Y, Wang Z, Wang Y, et al. Local magnetic spin mismatch promoting photocatalytic overall water splitting with exceptional solar-to-hydrogen efficiency[J]. Energy & Environmental Science, 2022, 15(1): 265-277.

[60] Kim C, Lee S, Kim S H, et al. Cobalt–iron–phosphate hydrogen evolution reaction electrocatalyst for solar-driven alkaline seawater electrolyzer[J]. Nanomaterials, 2021, 11(11): 2989.

[61] Pehlivan I B, Atak G, Niklasson G A, et al. Electrochromic solar water splitting using a cathodic WO3 electrocatalyst[J]. Nano Energy, 2021, 81: 105620.

[62] Roh H, Jung H, Choi H, et al. Various metal (Fe, Mo, V, Co)-doped Ni_2P nanowire arrays as overall water splitting electrocatalysts and their applications in unassisted solar hydrogen production with STH 14%[J]. Applied Catalysis B: Environmental, 2021, 297: 120434.

[63] Zhong Y, Lu Y, Pan Z, et al. Efficient Water Splitting System Enabled by Multifunctional Platinum-Free Electrocatalysts[J]. Advanced Functional Materials, 2021, 31(20): 2009853.

[64] Lu X, Lalwani S, Yuan L, et al. Accelerated bubble departure and reduced overpotential with nanoengineered porous bifunctional Ni_5P_4 electrocatalyst for PV-driven water splitting[J]. International Journal of Hydrogen Energy, 2022, 47(86): 36504-36516.

[65] Sun P, Zhou Y, Li H, et al. Round-the-clock bifunctional honeycomb-like nitrogen-doped carbon-decorated Co_2P/Mo_2C-heterojunction electrocatalyst for direct water splitting with 18.1% STH efficiency[J]. Applied Catalysis B: Environmental, 2022, 310: 121354.

[66] Zhang H, Aierke A, Zhou Y, et al. A high-performance transition-metal phosphide electrocatalyst for converting solar energy into hydrogen at 19.6% STH efficiency[J]. Carbon Energy, 2023, 5(1): e217.

[67] Zhang H, Zhou Y, Xu M, et al. Interface engineering on amorphous/crystalline hydroxides/sulfides heterostructure nanoarrays for enhanced solar water splitting[J]. ACS nano, 2022, 17(1): 636-647.

[68] Zhang H, Bi Z, Sun P, et al. Dense crystalline/amorphous phosphides/oxides interfacial sites for enhanced industrial-level large current density seawater oxidation[J]. ACS nano, 2023, 17(16): 16008-16019.